



# Repulsive photons in a quantum nonlinear medium

Sergio H. Cantu<sup>1,2,5</sup>, Aditya V. Venkatramani<sup>3,5</sup>, Wenchao Xu<sup>1,2</sup>, Leo Zhou<sup>3</sup>, Brana Jelenković<sup>4</sup>, Mikhail D. Lukin<sup>3</sup> and Vladan Vuletić<sup>1,2</sup>

**The ability to control strongly interacting light quanta (photons) is of central importance in quantum science and engineering<sup>1–5</sup>. Recently it was shown that such strong interactions can be engineered in specially prepared quantum optical systems<sup>6–10</sup>. Here, we demonstrate a method for coherent control of strongly interacting photons, extending quantum nonlinear optics into the domain of repulsive photons. This is achieved by coherently coupling photons to several atomic states, including strongly interacting Rydberg levels in a cold Rubidium gas. Using this approach we demonstrate both repulsive and attractive interactions between individual photons and characterize them by the measured two- and three-photon correlation functions. For the repulsive case, we demonstrate signatures of interference and self ordering from three-photon measurements. These observations open a route to study strongly interacting dissipative systems and quantum matter composed of light such as a crystal of individual photons<sup>11,12</sup>.**

Strong interactions between individual photons can be realized by coherently coupling them to strongly interacting Rydberg states inside an atomic gas using electromagnetically induced transparency (EIT)<sup>13,14</sup>. Inside this optical medium, the photons travel as coupled excitations of light and matter called dark-state polaritons, and inherit interactions from their atomic components<sup>15,16</sup>. When the medium is optically dense, the polariton propagates as a massive particle with a velocity that is much smaller than the speed of light, and interacts with other polaritons via the Rydberg atomic component<sup>17</sup>. This approach has been used to create absorptive nonlinearities<sup>8,18</sup>, attractive interactions, resulting in the formation of two- and three-photon bound states<sup>14,19</sup>, and transistors<sup>20,21</sup> at the single-photon level. At the same time, the realization of strong repulsive interactions, which are of interest for many potential applications in quantum metrology, quantum information and quantum simulation of certain Hamiltonians<sup>11,12,22</sup>, have proved much more challenging<sup>23</sup>.

Here, we demonstrate a novel method for coherent control of strongly interacting photons, extending quantum nonlinear optics into the domain of repulsive photons. To circumvent the high laser power requirements for repulsion in previous Rydberg–EIT schemes<sup>23</sup>, we make a simple extension to a four-level configuration (Fig. 1a,b) that couples probe photons to two distinct long-lived atomic states via two distinct two-photon processes. One of these long-lived states is a Rydberg state  $|r\rangle$  that enables interactions between photons. The other is a long-lived hyperfine state  $|f\rangle$  of the ground-state manifold that provides additional control over the particle's group velocity and effective mass<sup>24,25</sup>. A transmission spectrum for the probe photons in this scheme

(Fig. 1c) shows two nearly degenerate EIT resonances, corresponding to the two-photon resonances with states  $|r\rangle$  and  $|f\rangle$ . Such a double-EIT scheme results in the formation of two dark-state branches  $|d_0\rangle$  and  $|d_1\rangle$  with strongly modified dispersion, as can be seen in Fig. 1d. These dark-state branches combine both the interacting  $|r\rangle$  and the non-interacting  $|f\rangle$  states, allowing us to control the effective interactions. The inverse of the slope and the curvature of the dispersion relation determine the group velocities ( $v_{d_0}$ ,  $v_{d_1}$ ) and masses ( $m_{d_0}$ ,  $m_{d_1}$ ) of these two dark states, respectively. The propagation dynamics and nonlinear interactions arising from Rydberg components further result in a strong mixing between polaritons  $|d_0\rangle$  and  $|d_1\rangle$ . This coupling between the two polariton states and the resulting modified dispersion provide the necessary flexibility to control separately the effective potential between photons and their effective mass. The inset to Fig. 1d shows a case where increasing the coupling  $\Omega_f$  to  $|f\rangle$  switches the effective potential between photons from negative to positive, while their effective mass remains positive. Such tunability allows us to generate both attractive and repulsive interactions.

Our experiments utilize a dense gas of cold <sup>87</sup>Rb atoms in a crossed optical dipole trap (Fig. 1a). This results in an ellipsoidal atomic cloud with the dimensions root-mean-squared axial width of 8  $\mu\text{m}$  and radial width of 32  $\mu\text{m}$  with an optical depth of  $\sim 30$ . The atoms are optically pumped into the hyperfine state,  $F$ , and magnetic sub-level,  $m_F$   $|g\rangle = |5S_{1/2}, F = 1, m_F = 1\rangle$  of the electronic ground state (Fig. 1b). A weak probe field at 780 nm off-resonantly couples the state  $|g\rangle$  to the electronic excited state  $|p\rangle = |5P_{3/2}, F = 2, m_F = 2\rangle$  off-detuned by  $\Delta$ . The  $|p\rangle$  state is coupled to two meta-stable states: a Rydberg state  $|r\rangle = |73S_{1/2}, m_J = 1/2\rangle$  by a control beam at 479 nm, resulting in strong van der Waals interactions; and a non-interacting ground-state hyperfine sublevel  $|f\rangle = |5S_{1/2}, F = 2, m_F = 2\rangle$  by another control beam at 780 nm, off-detuned relative to the two-photon frequency by  $\delta_f$  and  $\delta_p$ , respectively. This coupling scheme results in the double-peaked transmission spectrum shown in Fig. 1c.

To characterize quantum nonlinear effects, photon–photon correlation functions are measured. Photons are uncorrelated as they enter the medium, but as they propagate, the strength of the interactions and the total travel time in the medium shape the amplitude and phase features while inside the medium. As dispersion outside the atomic medium is negligible, all of these features are preserved outside and can be detected in the form of photon number and phase correlations. We split the transmitted probe beam equally into three paths (Fig. 1a). This allows us to measure the two- and three-photon correlation functions  $g^{(2)}(\tau)$  or  $g^{(3)}(\tau_{21}, \tau_{31})$  as needed.  $\tau$  is the time separation between two photons and  $\tau_{21}$  and  $\tau_{31}$  are the time separations between the pairs of photons. For the phase correlations, we can additionally mix a frequency-

<sup>1</sup>Department of Physics, Massachusetts Institute of Technology, Cambridge, MA, USA. <sup>2</sup>Research Laboratory of Electronics, Massachusetts Institute of Technology, Cambridge, MA, USA. <sup>3</sup>Department of Physics, Harvard University, Cambridge, MA, USA. <sup>4</sup>Photonics Center, Institute of Physics, University of Belgrade, Belgrade, Serbia. <sup>5</sup>These authors contributed equally to this work: Sergio H. Cantu, Aditya V. Venkatramani. ✉e-mail: [lukin@physics.harvard.edu](mailto:lukin@physics.harvard.edu); [vuletic@mit.edu](mailto:vuletic@mit.edu)

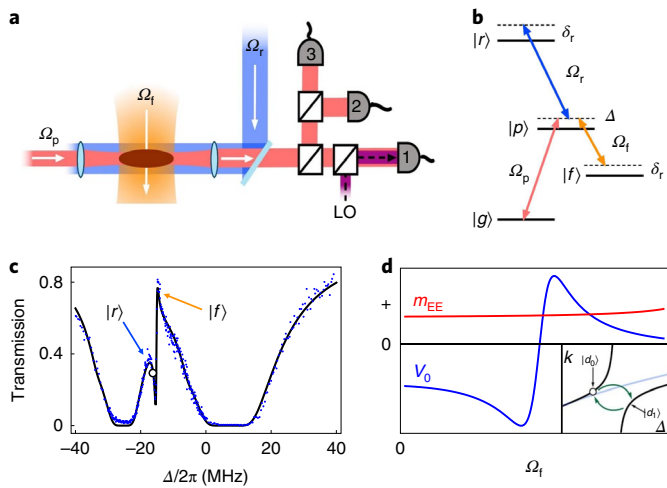


**Fig. 1 | Photon interaction engineering.** **a, b**, Experimental set-up (**a**) and level structure (**b**). A weak probe field (red) is coupled to the Rydberg state  $|r\rangle$  by a counter-propagating control field (blue) and to a non-interacting hyperfine ground state  $|f\rangle$  by a secondary control field (orange) applied perpendicularly. Probe photons are split onto three single-photon detectors numbered 1, 2 and 3 for correlation measurements. A local oscillator (LO) can be superimposed onto one of the detector paths to perform conditional phase measurements. **c**, The transmission spectrum of the probe. The two peaks correspond to the two-photon EIT resonances with  $|r\rangle$  and  $|f\rangle$ , respectively, where  $\Omega_r/2\pi = 20$  MHz,  $\Omega_f/2\pi = 10$  MHz,  $\delta_r/2\pi = (17 + \Delta)$  MHz and  $\delta_f/2\pi = (15 + \Delta)$  MHz. The solid black line is a fit to the data. The white dot is a representative repulsion point with single-photon transmission of 30%. **d**, Interaction crossover in the four-level system. Increasing the coupling to the non-interacting state  $|f\rangle$ , the effective potential amplitude,  $V_0$  (blue curve), flips sign while the sign of the effective mass of the photons,  $m_{EE}$  (red curve), remains the same. Inset: dispersion relation (momentum  $k$  versus  $\Delta$ ) for **c** at  $\Delta/2\pi = -16$  MHz (white dot) showing the two dark branches  $|d_0\rangle$  and  $|d_1\rangle$  (black lines). This dispersion is strongly modified with respect to the conventional three-level EIT with  $|r\rangle$  (blue curve) due to coupling to the non-interacting state  $|f\rangle$ . Dynamics due to propagation and Rydberg interactions further mix  $|d_0\rangle$  and  $|d_1\rangle$ , which allows us to control the effective potential amplitude,  $V_0$ , and effective mass,  $m_{EE}$ , of photons.

shifted probe into one of the paths to act as a local oscillator. We perform a heterodyne measurement to extract the conditional two-photon phase  $\phi^{(2)}(\tau)$ , which is the phase of a photon conditioned on detecting another photon at time  $\tau$  away. (See Supplementary Information for details.)

Figure 2 shows measurements of the two-photon correlation function  $g^{(2)}$  for different parameters corresponding to regimes of attractive or repulsive interactions. Figure 2a presents evidence of photon repulsion in the form of an antibunching feature with a value  $g^{(2)}(0) = 0.42 \pm 0.02$ . The likelihood of finding two photons is suppressed at  $\tau = 0$ , but then peaks at a finite temporal separation defined as  $\tau_R$ , indicating that the photons have been pushed away from each other (see the insets in Fig. 2). Indeed, we observe that  $g^{(2)}$  exceeds unity at later times with a peak value  $1.42 \pm 0.04$  at a temporal separation  $\tau_R = (0.10 \pm 0.02)$   $\mu$ s. Here, the one-photon detuning  $|\Delta|/2\pi = 10$  MHz is larger than the decay rate of the state  $|e\rangle$ ,  $\Gamma/2\pi = 6.1$  MHz, ensures that the dissipative nonlinear effects are too small to affect the observed features of  $g^{(2)}$ . At different detuning parameters, Fig. 2b demonstrates photon attraction where we measure  $g^{(2)}(0)$  to be bunched with a value  $g^{(2)}(0) = 2.6 \pm 0.08$ , indicating enhanced likelihood to find two photons at the same position. In addition to  $g^{(2)}$ , the two-photon phase  $\phi^{(2)}$  is measured to verify the coherent nature of the interactions. For both cases, we observe a

negative conditional two-photon phase at zero time separation  $\tau = 0$ , with values  $\phi^{(2)}(\tau = 0) = (-0.66 \pm 0.02)$  rad for the repulsive case and  $(-0.52 \pm 0.02)$  rad for the attractive case. This non-zero value of the conditional two-photon phase provides further evidence that the observed correlation features are due to coherent interactions, and not from nonlinear dissipation. The physical origin of the sign of the interaction is explained with an effective theoretical description presented below. The solid lines in Fig. 2 show the results of a full theoretical model (see Supplementary Information), in which we numerically solve the set of propagation equations for the light field and atomic coherences. These simulations are in good agreement with our experimental results.

To provide more intuitive insight into the observed behaviour of  $g^{(2)}$  and  $\phi^{(2)}$ , we derive an effective theoretical description. Our scheme features two propagating dark states  $|d_0\rangle$  and  $|d_1\rangle$ . Since they are nearly degenerate, they are coupled to each other<sup>26</sup>. Thus, we use a two-component wavefunction to describe the propagation dynamics in the system,  $\Psi(Z, z) \equiv \begin{pmatrix} \psi_1(Z, z) \\ \psi_2(Z, z) \end{pmatrix}$ , where  $Z$  is the mean

position of the two excitations and  $z$  is their spatial separation. The basis of  $\Psi(Z, z)$  is chosen such that the effective mass matrix  $M$  is diagonal, which allows one to interpret  $\Psi(Z, z)$  as propagating massive particles. Furthermore,  $\psi_1(Z, z)$  is proportional to the two-photon field amplitude  $EE(Z, z)$ , which allows us to directly compare the predictions to the observed photon dynamics (see Supplementary Information). The dynamics of  $\Psi(Z, z)$  are shown to be governed by a two-component Schrödinger-like equation:

$$i v_{\text{avg}} \partial_Z \Psi(Z, z) = -\frac{1}{2} M^{-1} \partial_z^2 \Psi(Z, z) + (E_0 + E_v \tilde{V}(z)) \Psi(Z, z), \quad (1)$$

where  $v_{\text{avg}}$  is the dark-states' average group velocity  $(v_{d_0} + v_{d_1})/2$ ,  $E_0$  is the non-interacting energy matrix,  $E_v$  is the interaction matrix and  $\tilde{V}(z)$  is the effective potential. Coupling between  $\psi_1(Z, z)$  and  $\psi_2(Z, z)$  manifests as off-diagonal terms in  $E_0$  and  $E_v$ , the latter of which arises from Rydberg interactions. The van der Waals interaction between Rydberg states  $V(z) = C_6/z^6$  is renormalized to yield the step-like effective potential with height  $V_0$  given by  $\tilde{V}(z) = \frac{V(z)}{1 + V(z)/V_0}$  (ref. 17). When the interaction shifts the Rydberg state away from resonance by an EIT linewidth, it eliminates transparency and saturates the effective potential. The diagonal terms of  $E_v$  are always positive, allowing us to adjust the sign of the effective potential via  $V_0$ . The effective mass for  $\psi_1 \propto EE$  is equal to the reduced mass  $m_{EE} = m_{d_0} m_{d_1} / (m_{d_0} + m_{d_1})$  of the dark-state excitations.

The observed repulsion and attraction in Fig. 2 can be understood from equation (1) by considering the signs of  $V_0$  and  $m_{EE}$  as one would in a standard Schrödinger equation. In the case of repulsion we have the product  $m_{EE} V_0 > 0$ , and in the case of attraction we have  $m_{EE} V_0 < 0$ . However, the coupling between  $\psi_1$  and  $\psi_2$  in this double-EIT scheme offers richer dynamics compared to a conventional EIT scheme, where only one dark-state branch exists. The signs of the effective potential and the effective mass for  $\psi_1$  are good qualitative indicators of the interactions, but the coupling to  $\psi_2$  is crucial to describe the full dynamics. To see this, we scan the two-photon detuning  $\delta_p$ , with  $\delta_i = -\delta_p$ , at fixed one-photon detuning  $\Delta/2\pi = -16$  MHz (Fig. 3). Within the scanned range, both  $m_{EE}$  and  $V_0$  remain positive, and therefore we expect repulsion between photons. Indeed, we observe zero-time antibunching  $g^{(2)}(0)$  and delayed-time positive correlations  $g^{(2)}(\tau_R) > 1$  (Fig. 3a). However, the zero-time phase  $\phi^{(2)}(0)$  switches from negative to positive as  $\delta_r$  increases (Fig. 3b). This switch is captured by the full theoretical model and also the effective model (see Supplementary Information). Such a sign flip of  $\phi^{(2)}(0)$  with the signs of  $V_0$  and  $m_{EE}$  unchanged is absent in a one-component Schrödinger-like description<sup>14</sup>.

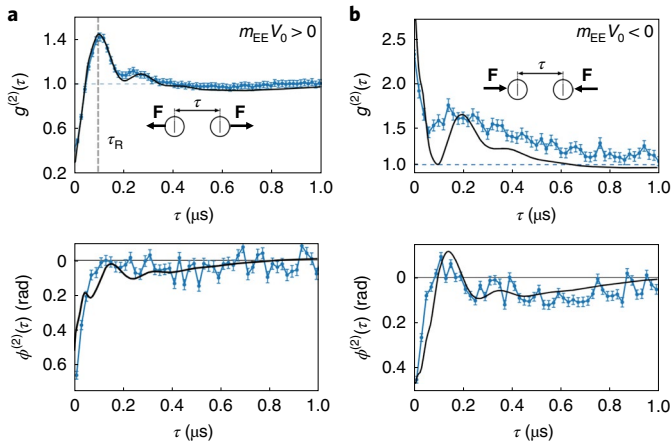


**Fig. 2 | Correlation functions showing repulsion and attraction.** The panels show the two-photon correlation function  $g^{(2)}(\tau)$  and two-photon phase  $\phi^{(2)}(\tau)$ , where  $\tau$  is the time separation between the two photons. **a**, Photon repulsion.  $g^{(2)}(0) = 0.42 \pm 0.02$  is antibunched and peaks at a later time  $\tau_R = (0.10 \pm 0.02) \mu\text{s}$  with a value of  $1.42 \pm 0.04$  compared to the uncorrelated value of 1 shown by the blue line. **b**, Photon attraction.  $g^{(2)}(0) = 2.6 \pm 0.08$  is bunched. The two-photon phase is negative at  $\tau = 0$  for both with values  $\phi^{(2)}(0) = (-0.66 \pm 0.02) \text{ rad}$  and  $(-0.52 \pm 0.02) \text{ rad}$  for the repulsion and attraction data, respectively. Both data are taken at the parameters  $\Omega_i/2\pi = 20 \text{ MHz}$ ,  $\Omega_j/2\pi = 10 \text{ MHz}$ ,  $\delta_i/2\pi = 1.1 \text{ MHz}$ ,  $\delta_j/2\pi = -1.1 \text{ MHz}$  and with  $\Delta/2\pi = -10 \text{ MHz}$  for repulsion and  $\Delta/2\pi = 10 \text{ MHz}$  for attraction. The black solid line is a theory simulation of the system by propagating the two-particle optical Bloch equations. Simulations use experimental parameters, but  $\Omega_i/2\pi$  is increased to 12 MHz to fit the data. The error bars indicate one standard deviation (s.d.). For attractive interactions, two-photon loss processes are not captured by the optical Bloch equations, which accounts for the reduced contrast in the oscillation in the experimental  $g^{(2)}$  data relative to the one shown in the simulated  $g^{(2)}$ . **F**, force between two photons.

$N$ -particle correlations can serve as a powerful tool to characterize emerging self-ordered phases of matter<sup>27</sup>. In our system, we further investigate the quantum dynamics of repulsively interacting photons by measuring the third-order correlation function  $g^{(3)}(\tau_{21}, \tau_{31})$ . The experimentally measured  $g^{(3)}$  for the same parameters used to measure  $g^{(2)}$  in Fig. 2a is shown in Fig. 4a. We show  $g^{(3)}$  as the two-dimensional correlations of detecting three photons

arriving with time separations  $\tau_{21}$  and  $\tau_{31}$ . Just as in the case of the  $g^{(2)}$  measurement, when two photons are detected together ( $\tau_{21} = 0$ ,  $\tau_{31} = 0$  or  $\tau_{21} - \tau_{31} = 0$  corresponding to the vertical, horizontal and diagonal lines), we observe repulsion features of antibunching (red) followed by positive correlations (blue) at a separation of  $\tau_R$ .

To investigate interference effects between three photons, we analyse the situation where two photons are detected with a time separation  $2\tau'$ , and plot in Fig. 4b the likelihood to detect the third photon detected at time  $\tau$  from their midpoint. We define this normalized correlation as  $g^{(1+2)}(\tau, 2\tau')$ , corresponding to  $g^{(3)}(\tau' + \tau, 2\tau')$  (averaged over all permutations) normalized by the two-photon correlation  $g^{(2)}(2\tau')$ . Figure 4b shows  $g^{(1+2)}$  for a few different time separations  $\tau'$ . For long time separations ( $\tau' > 2\tau_R$ ), the third photon experiences repulsion near either photon of the pair independently. For very short time separations ( $\tau' \sim 0$ ), the third photon experiences a much stronger repulsion from the pair than what we observe in  $g^{(2)}$ , as evidenced by the enhancement of both the antibunching ( $0.18 \pm 0.04$ ) and bunching ( $2.37 \pm 0.16$ ) features of  $g^{(1+2)}$ . Compared to the peak value of  $g^{(2)}$  ( $1.42 \pm 0.04$ ), the deviation from 1 is more than twice larger. This indicates that the three-photon system is governed by three-photon wavefunction interference, rather than a statistical mixture of two-photon repulsive processes. As the pair separates, the third photon gets pushed from either side, which increases its likelihood of being localized in between the two other photons. Figure 4c plots the likelihood of three photons detected with an equal interval separated by  $\tau'$  by scanning  $g^{(1+2)}(0, 2\tau')$ . As  $\tau'$  reaches the time separation  $\tau_R$ , the third photon is most likely to be in the middle of the other two photons with a maximum value of  $g^{(1+2)}(0, 2\tau') = 1.76 \pm 0.2$ , near  $2\tau_R$  within experimental uncertainty. This indicates the presence of coherent three-photon wavefunction interference, and hints at the onset of crystallization of photons mediated through repulsive interactions.

The ability to tune photon-photon interactions across attractive and repulsive regimes provides an opportunity for extensive control of strongly interacting photons in both one dimension and higher dimensions. This opens avenues to studying exotic phases of matter<sup>28</sup>, including self-organization in open quantum systems<sup>3</sup>, as well as photonic quantum materials that cannot be realized with conventional quantum systems. Many-body states such as photon crystals can enable new applications in quantum metrology and quantum communication<sup>11,12</sup>. The extension to higher dimensions can be accomplished by carefully shaping the probing laser using spatial light modulators<sup>29</sup>. By engineering the effective mass and interactions along different dimensions, it might be possible to

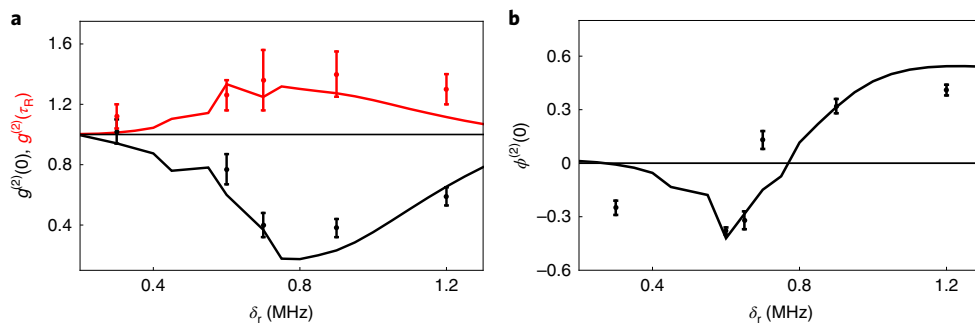


**Fig. 3 | Repulsive interactions and phase.** **a**, Repulsive interactions as indicated by antibunching at  $g^{(2)}(0) < 1$  and peak  $g^{(2)}(\tau_R) > 1$ . Results from full theoretical simulations are shown as solid black lines. Experimental parameters:  $\Omega_i/2\pi = 23 \text{ MHz}$ ,  $\Omega_j/2\pi = 10 \text{ MHz}$ ,  $\Delta/2\pi = -16 \text{ MHz}$ , and with  $\delta_i = -\delta_j$ .  $\Omega_i$  is increased to 11 MHz in the theoretical simulation to fit the data and  $\delta_i$  is corrected for a Stark shift arising from imperfect polarization (see Supplementary Information for details). For these parameters, we have  $m_{EE}$  and  $V_0$  remain positive, implying repulsion as discussed in the main text. **b**, The zero-time phase correlation  $\phi^{(2)}(0)$  changes from negative to positive even when the signs of  $m_{EE}$  and  $V_0$  do not change, illustrating the need for a two-component wavefunction. The error bars indicate one s.d.

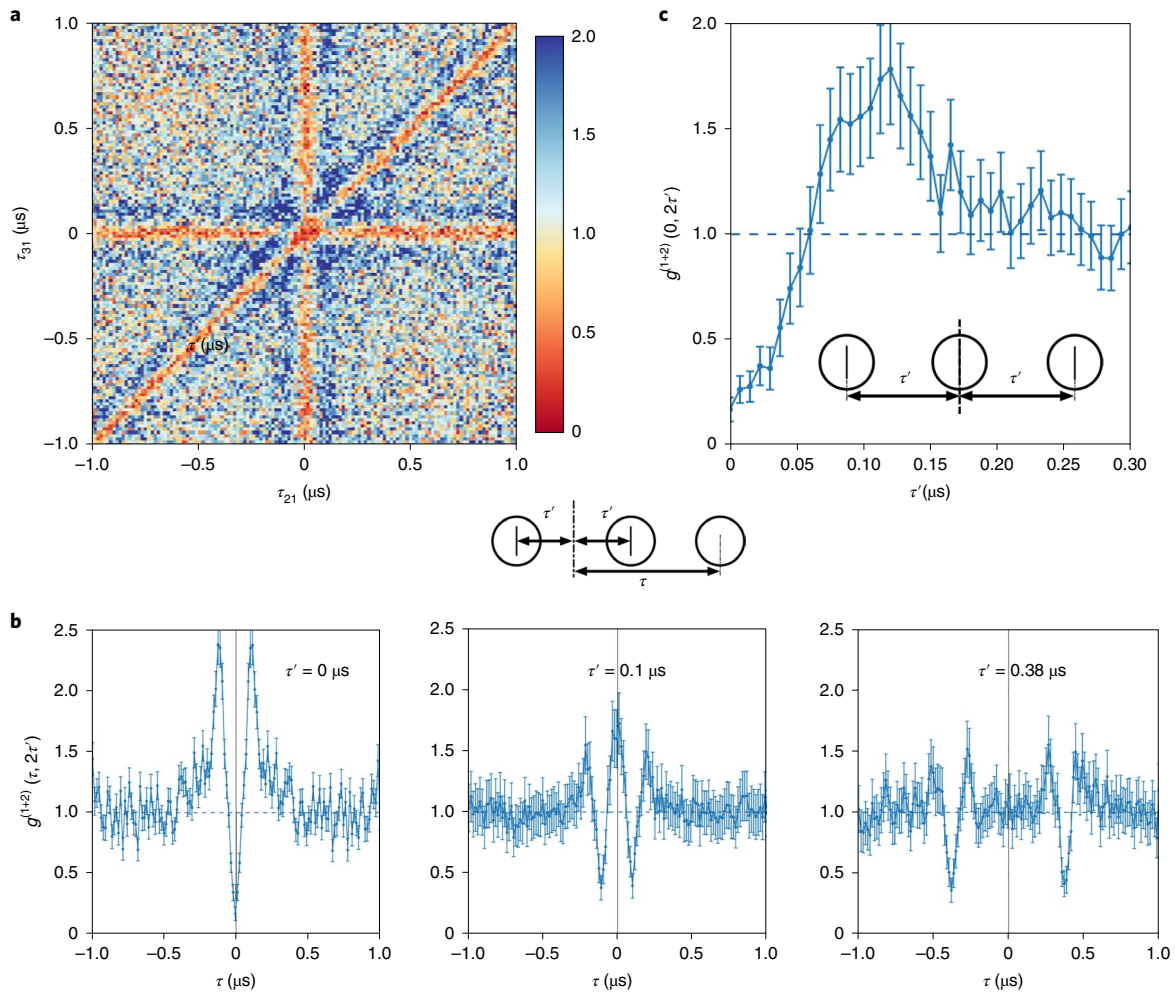


**Fig. 4 | Three-photon correlations and onset of crystal-like behaviour.** **a**, A two-dimensional projection of the three-photon correlation function  $g^{(3)}(\tau_{21}, \tau_{31})$  for the same parameters as in Fig. 2a. **b**, The likelihood of detecting a photon at a separation of  $\tau$  from the midpoint of two other photons detected with separation  $2\tau'$ :  $g^{(1+2)}(\tau, 2\tau') = g^{(3)}(\tau + \tau', 2\tau')/g^{(2)}(2\tau')$ . Probabilities are shown for  $2\tau' = 0.00(1), 0.20(1), 0.76(1)$   $\mu\text{s}$ , indicating three-photon wavefunction interference. See the text for discussion. **c**, The likelihood of three photons detected at equal intervals to be  $\tau'$ , which is maximum near the characteristic timescale  $\tau_R = (0.10 \pm 0.02)$   $\mu\text{s}$ . The error bars indicate one s.d.

sustain photonic Efimov states when using all-attractive forces or study topological physics with photons<sup>30</sup>.

Received: 22 October 2019; Accepted: 23 April 2020;

Published online: 01 June 2020

## References

- Hartmann, M., Brandao, F. & Plenio, M. Strongly interacting polaritons in coupled arrays of cavities. *Nat. Phys.* **2**, 849–855 (2006).
- Greentree, A., Tahan, C., Cole, J. & Hollenberg, L. Quantum phase transitions of light. *Nat. Phys.* **2**, 856–861 (2006).
- Ma, R. et al. A dissipatively stabilized Mott insulator of photons. *Nature* **566**, 51–57 (2019).
- Clark, L. W. et al. Interacting Floquet polaritons. *Nature* **571**, 532–536 (2010).
- Giovannetti, V., Lloyd, S. & Maccone, L. Advances in quantum metrology. *Nat. Photon.* **5**, 222–229 (2011).
- Friedler, I., Petrosyan, D., Fleischhauer, M. & Kurizki, G. Long-range interactions and entanglement of slow single-photon pulses. *Phys. Rev. A* **72**, 043803 (2005).
- Birnbaum, K. M. et al. Photon blockade in an optical cavity with one trapped atom. *Nature* **436**, 87–90 (2005).
- Dudin, Y. O. & Kuzmich, A. Strongly interacting Rydberg excitations of a cold atomic gas. *Science* **336**, 887–889 (2012).
- Hacker, B., Welte, S., Rempe, G. & Ritter, S. A photon–photon quantum gate based on a single atom in an optical resonator. *Nature* **536**, 193–196 (2016).
- Busche, H. et al. Contactless nonlinear optics mediated by long-range Rydberg interactions. *Nat. Phys.* **13**, 655–658 (2017).
- Chang, D. et al. Crystallization of strongly interacting photons in a nonlinear optical fibre. *Nat. Phys.* **4**, 884–889 (2008).
- Otterbach, J., Moos, M., Muth, D. & Fleischhauer, M. Wigner crystallization of single photons in cold Rydberg ensembles. *Phys. Rev. Lett.* **111**, 113001 (2013).
- Liang, Q. Y. et al. Observation of three-photon bound states in a quantum nonlinear medium. *Science* **359**, 783–786 (2018).
- Firstenberg, O. et al. Attractive photons in a quantum nonlinear medium. *Nature* **502**, 71–75 (2013).
- Chang, D., Vuletic, V. & Lukin, M. Quantum nonlinear optics - photon by photon. *Nat. Photon.* **8**, 685–694 (2014).
- Lukin, M. D. et al. Dipole blockade and quantum information processing in mesoscopic atomic ensembles. *Phys. Rev. Lett.* **87**, 037901 (2001).
- Gorshkov, A. V., Otterbach, J., Fleischhauer, M., Pohl, T. & Lukin, M. D. Photon–photon interactions via Rydberg blockade. *Phys. Rev. Lett.* **107**, 133602 (2011).
- Peyronel, T. et al. Quantum nonlinear optics with single photons enabled by strongly interacting atoms. *Nature* **488**, 57–60 (2012).
- Stiesdal, N. et al. Observation of three-body correlations for photons coupled to a Rydberg superatom. *Phys. Rev. Lett.* **121**, 103601 (2018).
- Tiarks, D., Baur, S., Schneider, K., Dürr, S. & Rempe, G. Single-photon transistor using a Förster resonance. *Phys. Rev. Lett.* **113**, 053602 (2014).
- Gorniaczyk, H., Tresp, C., Schmidt, J., Fedder, H. & Hofferberth, S. Single-photon transistor mediated by interstate Rydberg interactions. *Phys. Rev. Lett.* **113**, 053601 (2014).

22. Sommer, A., Büchler, H. P. & Simon, J. Quantum crystals and Laughlin droplets of cavity Rydberg polaritons. Preprint at <https://arxiv.org/abs/1506.00341> (2015).
23. Bienias, P. et al. Scattering resonances and bound states for strongly interacting Rydberg polaritons. *Phys. Rev. A* **90**, 053804 (2014).
24. Lukin, M. D., Yelin, S. F., Fleischhauer, M. & Scully, M. O. Quantum interference effects induced by interacting dark resonances. *Phys. Rev. A* **60**, 3225–3228 (1999).
25. Mahmoudi, M., Fleischhaker, R., Sahrai, M. & Evers, J. Group velocity control in the ultraviolet domain via interacting dark-state resonances. *J. Phys. B* **41**, 025504 (2008).
26. Duan, L. M., Cirac, I. & Zoller, P. Geometric manipulation of trapped ions for quantum computation. *Science* **292**, 1695–1697 (2001).
27. Schauß, P. et al. Observation of spatially ordered structures in a two-dimensional Rydberg gas. *Nature* **491**, 87–91 (2012).
28. Schauß, P. et al. Crystallization in Ising quantum magnets. *Science* **347**, 1455–1458 (2015).
29. Nogrette, F. et al. Single-atom trapping in holographic 2D arrays of microtraps with arbitrary geometries. *Phys. Rev. X* **4**, 021034 (2014).
30. Ozawa, T. et al. Topological photonics. *Rev. Mod. Phys.* **91**, 015006 (2019).

**Publisher's note** Springer Nature remains neutral with regard to jurisdictional claims in published maps and institutional affiliations.

© The Author(s), under exclusive licence to Springer Nature Limited 2020

**Data availability**

Source data are available for this paper. All other data that support the plots within this paper and other findings of this study are available from the corresponding author upon reasonable request.

**Acknowledgements**

We acknowledge helpful conversations with T. Pohl and C. Murray. We also acknowledge help with control electronics from Z. Zhang.

**Author contributions**

The experiment and analysis were carried out by S.H.C., A.V.V., W.X. and B.J. Theoretical modelling was performed by L.Z. and A.V.V. All work was supervised

by M.D.L. and V.V. All authors discussed the results and contributed to the manuscript.

**Competing interests**

The authors declare no competing interests.

**Additional information**

**Supplementary information** is available for this paper at <https://doi.org/10.1038/s41567-020-0917-6>.

**Correspondence and requests for materials** should be addressed to M.D.L. or V.V.

**Reprints and permissions information** is available at [www.nature.com/reprints](http://www.nature.com/reprints).